Automatic Detection of InSAR Deformation and Tropospheric Noise Features Using Computer Vision: A Case Study Over West Texas

Scott Staniewicz[1] and **Jingyi Chen[1,2,3]**

[1]University of Texas at Austin, Aerospace Engineering and Engineering Mechanics, Austin, TX, USA, [2]University of Texas at Austin, Center of Space Research, Austin, TX, USA, [3]University of Texas at Austin, Earth and Planetary Sciences, Austin, TX, USA

Abstract Automatic detection of surface deformation features from large volumes of Interferometric Synthetic Aperture Radar (InSAR) data is challenging because the magnitude of InSAR measurement noise varies substantially in both space and time. In this work, we present a computer vision algorithm based on Laplacian of Gaussian (LoG) filtering to detect the size and location of unknown surface deformation features. Because our algorithm targets spatially coherent features, tropospheric noise artifacts with similar spatial characteristics may also be detected. To quantify the likelihood that a detected feature is a real deformation signal, we estimate the tropospheric noise spectrum directly from data, and we characterize tropospheric noise using noise simulations that resemble the actual InSAR observations. We demonstrate our algorithm using Sentinel-1 data acquired between 2014 and 2019 over the ~80,000 km^2 oil-producing Permian Basin in West Texas—one of the most productive oil fields in the world. We detect clusters of deformation features associated with oil production, wastewater injection, and fault activity. The number of detected deformation features increases substantially over the study period, which is consistent with the overall rise in oil production within the Permian Basin since 2014. Further, we show that our algorithm can detect subtle surface deformation from the 26 March 2020 M$_W$ 5.0 earthquake near Mentone, Texas, USA and quantify detection uncertainty. Our method is robust and flexible and can be integrated into various multi-temporal InSAR time series techniques for detecting a broad range of local deformation features.

Plain Language Summary Earth's surface can deform over time due to natural events such as earthquakes or volcanic eruptions, as well as human activities like oil and gas extraction. These subtle, centimeter-level changes can be captured using a satellite radar technique known as Interferometric Synthetic Aperture Radar (InSAR). However, residual tropospheric noise looks visually similar to real surface deformation, which may hinder accurate interpretation of InSAR results. To address this challenge, we present here an unsupervised computer vision algorithm to automatically detect spatially coherent features from an InSAR surface deformation map. Using the tropospheric noise spectrum derived from real InSAR data, we quantify the likelihood that a detected feature is a real deformation signal rather than tropospheric noise. We demonstrate our algorithm using both synthetic data and Sentinel-1 InSAR data over the Permian Basin in West Texas. Our results on cumulative deformation maps show an increased number of surface subsidence and uplift features well above the noise level, consistent with oil and gas production and wastewater injection activities reported in the area.

1. Introduction

Interferometric Synthetic Aperture Radar (InSAR) has made it possible to monitor surface deformation with 10–100s m spatial resolution and millimeter-to-centimeter accuracy over large geological basins (e.g., Chaussard et al., 2014; Chen et al., 2014, 2016; Pritchard & Simons, 2004). Since the launch of the Sentinel-1 mission in 2014, the quantity and quality of open-access InSAR data have grown enormously. Processing and interpreting such a large volume of InSAR data can benefit from artificial intelligence and computer vision automatic detection algorithms for identification of deformation hot spots without extensive manual inspection. However, this is a difficult algorithm design task because the expected deformation signals and noise artifacts can vary substantially at different study sites.

Previous studies developed algorithms for detecting deformation signals in pixel-wise InSAR deformation time series based on magnitude thresholds. Such thresholds can be set manually (Raspini et al., 2018), derived from

auxiliary data (e.g., global atmospheric weather models or MODIS water vapor measurements; Barnhart & Lohman, 2013; Parker et al., 2015), or estimated using simulated noise parameters (Havazli & Wdowinski, 2021). However, these pixel-wise approaches typically neglect the spatial correlation of deformation signals and tropospheric noise, limiting their effectiveness for identifying coherent deformation features. Alternatively, convolutional neural networks (CNNs) have been applied to individual interferograms (Anantrasirichai et al., 2018) or InSAR time series (Rouet-Leduc et al., 2021). However, these deep learning-based methods require labeled training data or simulated ground truth, and still face challenges distinguishing deformation from spatially coherent tropospheric noise (Hanssen, 2001). Therefore, most InSAR processing for deformation mapping includes a tropospheric noise mitigation stage.

Tropospheric noise, caused by changes in atmospheric pressure, temperature, or water vapor between the two radar acquisitions, has a spatially random (also called turbulence noise) and a systematic component that is stratified with topography. The stratified component may be mitigated using external data products, such as global atmospheric weather models or MODIS water vapor measurements (Cao et al., 2021; Parker et al., 2015) from measurements of zenith delay made by global navigation satellite systems (GNSS) (Yu et al., 2018). When the deformation of interest occurs away from large changes in topography and topographically-correlated deformation (Yang et al., 2024), or in cases where the turbulence dominates the tropospheric noise, empirical or statistical models can be used to mitigate the noise. These corrections may include a simple averaging/stacking (Sandwell & Price, 1998), more comprehensive spatio-temporal statistical modeling and filtering (Li et al., 2019; Liu et al., 2024; Y. Wang et al., 2022-06) or deep learning-based filtering (Rouet-Leduc et al., 2021; Zhao et al., 2021).

Despite advances in mitigation techniques, residual tropospheric noise can still mimic deformation signals, particularly in low signal-to-noise conditions with strong turbulence noise. Thus, quantifying uncertainty associated with these residual effects becomes essential for reliable automated deformation detection. Given the complexity and nonlinearity inherent in the interaction between tropospheric noise mitigation and automated detection algorithms, a purely analytical approach can be challenging. To address this, we propose a simple, data-driven method that employs synthetic sampling inspired by the Bootstrap resampling technique (Efron & Tibshirani, 1994; Olsen et al., 2023). We estimate the tropospheric turbulence noise spectrum directly from the InSAR data (Tymofyeyeva & Fialko, 2015; Zebker et al., 2023), enabling us to generate realistic synthetic noise samples (Hanssen, 2001). These synthetic samples allow us to robustly estimate the likelihood that detected features originate from residual tropospheric noise. Our approach incorporates a Laplacian of Gaussian (LoG) filtering-based algorithm, inspired by feature detection methods in computer vision, such as the Scale Invariant Feature Transform (SIFT; Lindeberg, 1998; Lowe, 2004; Witkin, 1987). This method efficiently identifies spatially coherent deformation features without requiring labeled training data. We demonstrate our algorithm on a synthetic test and on real Sentinel-1 ascending and descending scenes acquired over an 80,000 km^2 oil-producing region in West Texas. We apply the techniques to both long-term cumulative deformation mapping and to a detection of transient subtle surface deformation due to the 26 March 2020 M$_W$ 5.0 earthquake near Mentone, TX. We show that our algorithm is flexible and can be integrated with different time series techniques to detect a broad range of deformation features above tropospheric noise level.

2. Methods

2.1. Overview

Under the assumption that tropospheric noise is the primary error source, our algorithm is designed to automatically identify spatially coherent deformation features in an InSAR surface deformation map. In cases where temporal decorrelation noise cannot be ignored, the Persistent Scatterers (PS) technique can be employed to identify high-quality radar pixels that suffer from minimal decorrelation artifacts (Ferretti et al., 2000; Hooper et al., 2004; Huang & Zebker, 2022; Shanker & Zebker, 2007; Wang & Chen, 2022). An interpolation between PS pixels can then be performed to reconstruct spatially coherent phase measurements (J. Chen et al., 2015) before applying the algorithm described in this paper.

As shown in Figure 1, the overall algorithm workflow can be divided into two stages. The inputs to both stages are the same set of unwrapped interferograms. During the first stage, a surface deformation map is derived from unwrapped interferograms using an existing InSAR processing algorithm (e.g., stacking (Sandwell & Price, 1998)
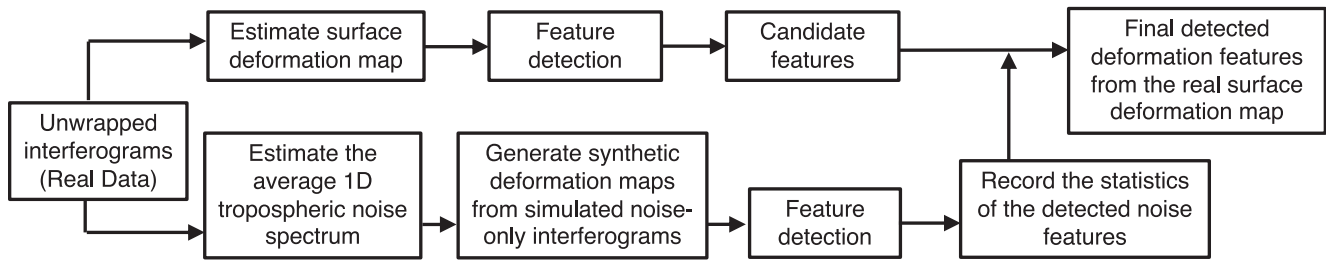
Figure 1. Overview of the algorithm workflow.

or the Small Baseline Subset algorithm as described in Berardino et al. (2002)). An automatic feature detection algorithm based on LoG filtering (Section 2.2) is then applied to identify spatially coherent features in the deformation map. To determine whether a detected feature is likely associated with a real deformation signal or tropospheric noise artifacts, the second stage focuses on the estimation of tropospheric noise characteristics of the InSAR data set. Here, common reference stacking (Tymofyeyeva & Fialko, 2015; Zebker et al., 2023) is employed to estimate tropospheric noise at each SAR acquisition time, from which the average tropospheric noise Power Spectral Density (PSD) is computed (Section 2.3). Synthetic surface deformation maps are then generated from simulated interferograms that (a) follow the tropospheric noise spectrum derived from real data, and (b) contain no deformation signals. The same feature-detection algorithm is applied to the synthetic noise-only surface deformation maps, and the characteristics of the detected noise features are recorded (Section 2.4). Finally, the statistics of detections from synthetic noise-only interferograms are used to determine which candidate features detected from the real deformation map are likely associated with real deformation signals.

2.2. Automatic Feature Detection

Given a raster surface deformation map M derived from InSAR phase observations, the value M_{ij} at the ith row and j^{th} column represents the magnitude of a cumulative, seasonal, or transient deformation signal at this pixel. Over natural terrain, the deformation signal of interest is often caused by geophysical processes, including but not limited to near-surface coastal processes, confined aquifer pumping and recharge, volcanism, and fault activities. Because the Earth's crust can be considered as a stratified elastic-viscoelastic medium, such surface displacements are typically spatially coherent (Segall, 2010). As a result, many commonly used InSAR phase unwrapping methods (e.g., Chen & Zebker, 2001) or time series analysis techniques employ similar assumptions that deformation signals vary slowly in space in order to separate them from decorrelation noise that is random in space (Zebker & Villasenor, 1992). In this study, our goal is to automatically detect such spatially coherent local deformation features in an InSAR deformation map M.

Computer vision algorithms have been developed to automatically detect features in 2D image data. One of the earliest successful algorithms demonstrated that filtering an image using a series of LoG filters could effectively detect spatially coherent features at multiple scales (Lindeberg, 1993). Although these methods are commonly referred to as blob detection algorithms by computer scientists, they can detect spatially coherent features of various shapes, not limited to blobs. Subsequent research focused on improving the computational efficiency of these algorithms for real-time computer vision applications. These improved filters often employ approximations of the LoG filter, such as the Difference of Gaussian (DoG) used in Lowe (2004), or filters more sensitive to corners and edges (e.g., the Determinant of Hessian (DoH) filter as described in the Scale-Invariant Feature Transform algorithm (Lindeberg, 1998). While the goal of many computer vision applications is to detect different types of stable image features, our objective is to detect only spatially coherent surface deformation features. Furthermore, the computational time required for feature detection is not a limiting factor, which constitutes a small fraction of the time required for interferogram formation and analysis. Therefore, we choose the LoG filter rather than its more computationally-efficient less-accurate approximations in the algorithm design.

An LoG kernel $K^{(m)}$ with a size σ_m is written as:

$$K_{ij}^{(m)} = \left(\frac{(i-l)^2 + (j-l)^2 - 2\sigma_m^2}{2\pi\sigma_m^4} \right) e^{-\frac{(i-l)^2+(j-l)^2}{2\sigma_m^2}} \tag{1}$$
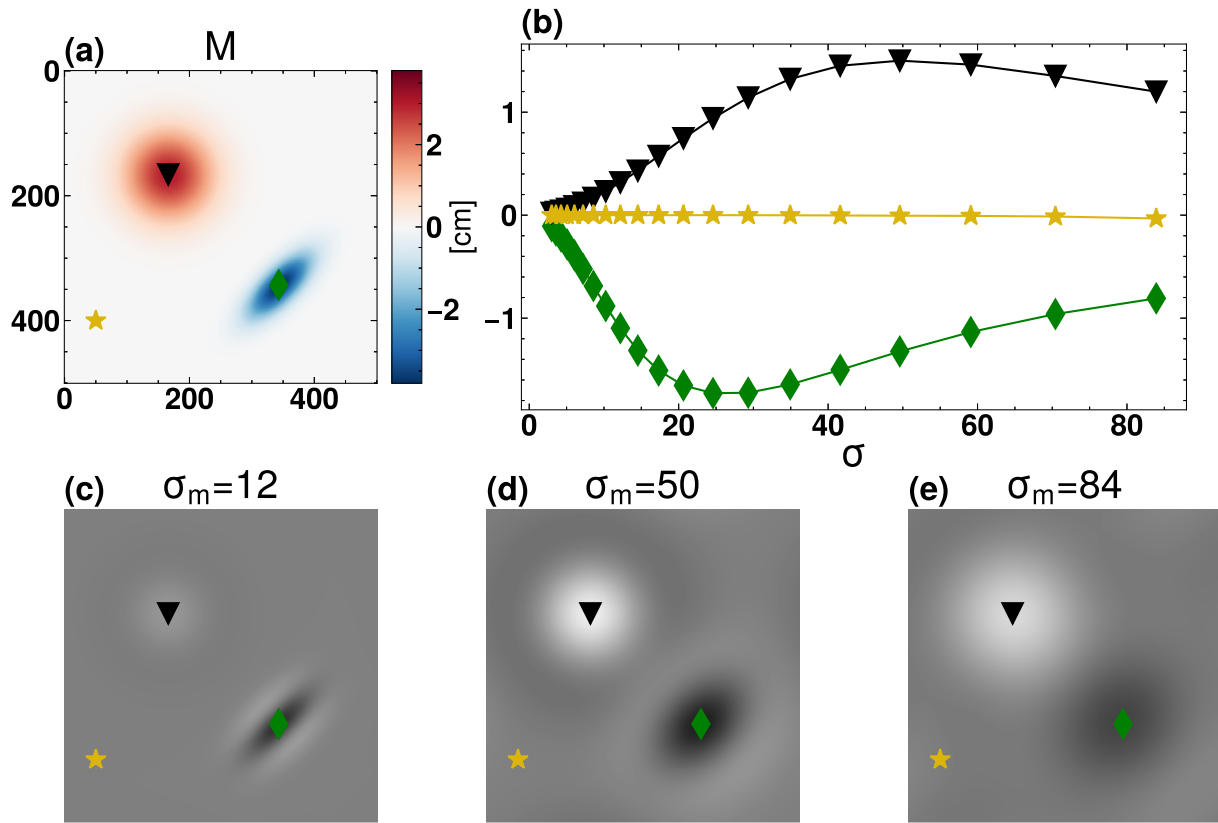
Figure 2. (a) A synthetic deformation map that contains one Gaussian-shaped uplift feature in the upper left and one elliptical Gaussian subsidence feature in the lower right. (b) Laplacian of Gaussian (LoG) response amplitudes for 20 filters with various sizes (σ_m) at three marker points. The marker locations are shown in panel (a). (c–e) The LoG filter responses for $\sigma_m = 12$, 50, and 84.

where pixel indices $ij \in \{0, 1, \ldots, 2l\}$. The unit of σ_m is given in pixels, which can be scaled to meters based on the pixel spacing of the InSAR deformation map M.

We generate a set of LoG kernels $K^{(1)}, K^{(2)}, \ldots$ with progressively larger σ_m (Figure S1 in Supporting Information S1), and calculate the mth filter response $L^{(m)}$ as:

$$L^{(m)} = M * K^{(m)} \tag{2}$$

Here $*$ denotes the 2D discrete convolution, which is typically computed using the Fast Fourier Transform (FFT) algorithm because of its superior computational efficiency (Szeliski, 2022).

To demonstrate how to estimate the size of a spatially coherent feature from the filter responses, Figure 2a shows a 500×500 synthetic deformation map M that contains one Gaussian-shaped uplift feature in the upper left and one elliptical Gaussian subsidence feature in the lower right. We filtered this deformation map using 20 LoG kernels of sizes ranging from $\sigma_1 = 3$ pixels to $\sigma_{20} = 100$ pixels with a base-2 logarithmic spacing, and the filter responses are shown in Figures 2b–2e. For the round uplift case, the filter response $L^{(m)}$ (the black curve in Figure 2b) is strongest when the kernel size σ_m matches the deformation feature radius r as $r = \sqrt{2}\sigma_m$. This is known as the extreme point, or the local maximum points of $|L^{(m)}|$ for all attempted σ_m. For the elliptical subsidence case, the extreme point is reached when the average length of the two primary axes of the deformation feature is $\sim\sqrt{2}\sigma_m$ (the green curve in Figure 2b). For the case of no deformation, no substantial filter response is generated for any filter size (the gold curve in Figure 2b).

In the case that two candidate features have substantial overlapping areas, the feature with smaller size may be discarded to suppress redundant detections (Figures 3a–3b). This is an optional user-defined step, given that the
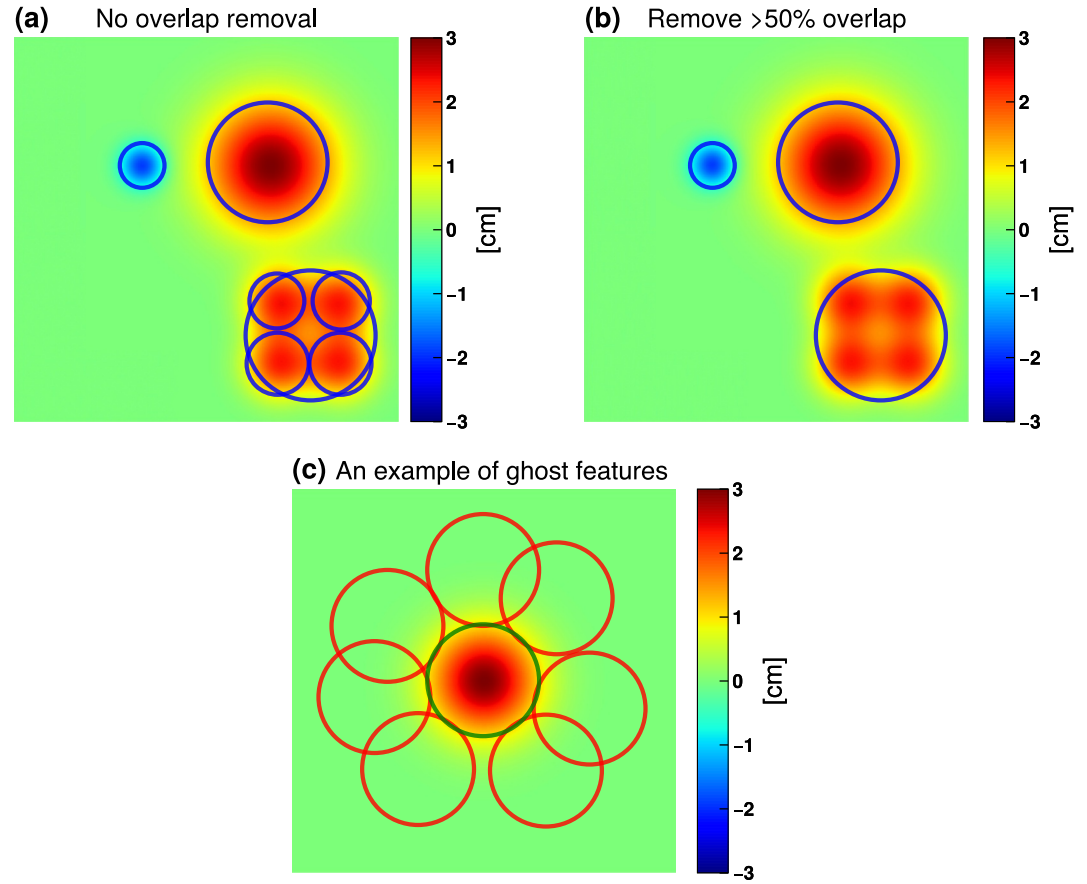
Figure 3. (a) An example synthetic deformation map. Four uplift features are also detected as one merged, larger feature. (b) The detection result after removing overlapping features (an optional step). (c) An example of false positive ghost features (red circles) detected at the edge of an uplift feature (the green circle). For the red ghost features (detected as "subsidence" features relative to the center uplift), the extreme amplitude values are located near the feature edge. For the green real uplift feature, the extreme amplitude values are located near the center. We use the distance from the center of the detection to the local extreme amplitude within the circle to identify and remove ghost features.

definition of redundant detections varies based on the objective of each InSAR deformation mapping application. e.g., this removal step may be configured to only remove features with a large overlap (e.g., >80%) and within a certain size range (deformation features with very different sizes are likely associated with different sources) to avoid removing nested deformation features (e.g., a small uplift feature located within broad regional subsidence patterns). Additionally, the LoG filter may falsely flag ghost features at the edges of a real deformation feature (Figure 3c). This is because deformation features with strong curvature at the center also contain a strong opposite-signed curvature near the border (Lindeberg, 1998). To remove those false positive ghost detections, we use the distance from the candidate feature's center to the deformation amplitude extremum as a measure. If the extreme amplitude is located near the edge of a feature, the detection is likely a false-positive feature. In our test case, we discarded features with local extremum distances larger than 75% of the feature radius, which effectively removed all false positives near the edge of real deformation features based on visual inspection in all Sentinel-1 test cases.

For the kth detected feature, our algorithm outputs the feature center location (i_k, j_k), the feature size r_k, the filter response magnitude $|g_k|$ at the extreme point, and the feature magnitude $|\overline{d_k}|$ defined as the weighted maximum magnitude of all pixels within the kth feature:

$$|\overline{d_k}| = \max_{kk}|w_{kk}M_{kk}| \tag{3}$$

Here the weight w_{kk} equals $\exp\left[-(r_{kk}/r_k)^2\right]$, where r_{kk} is the distance between a pixel within the feature and the feature center. Because of the exponential weighting, the feature magnitude $|\overline{d_k}|$ is mostly determined by the observed magnitudes near the center of a feature. We can exclude undesired detections below the noise level by setting thresholds on the filter response magnitude $|g_k|$, the feature magnitude $|\overline{d_k}|$, and feature size r_k. How to determine the noise level of an InSAR deformation map is the focus of the remaining method sections.

2.3. Tropospheric Noise Spectrum

InSAR measurement noise can also produce spatially coherent features that are detectable by our feature detection algorithm. Here we focus on characterizing the tropospheric turbulence noise in each SAR scene. This is because tropospheric turbulent noise (a) is correlated in space (Emardson et al., 2003; Lohman & Simons, 2005); (b) is present in all InSAR data sets with greatly varying magnitudes (Barnhart & Lohman, 2013; Hooper et al., 2012); and (c) is often the primary noise source that limits InSAR measurement accuracy (Bekaert et al., 2015; Jolivet et al., 2014; Parker et al., 2015).

Consider an interferogram formed using two SAR scenes acquired at times t_1 and t_2. In the case that tropospheric turbulence noise is the dominant noise term, the measured interferometric phase $\phi_{1,2}$ (in radians) at a pixel of interest can be written as (Zebker et al., 1997):

$$\phi_{1,2} \approx \frac{4\pi}{\lambda}(\alpha_2 - \alpha_1 + \Delta d_{1,2}) \tag{4}$$

where λ is the radar wavelength, α_1 and α_2 represent the tropospheric delay at the two SAR acquisition times t_1 and t_2, and $\Delta d_{1,2}$ is the Line-Of-Sight (LOS) deformation $(d_2 - d_1)$ between t_1 and t_2. The unit of λ, α_1, α_2, and $\Delta d_{1,2}$ is in centimeters. Here all the terms are relative measurements with respect to a local reference pixel rather than to an absolute geodetic reference frame.

Given N SAR acquisitions, we can estimate the tropospheric noise on the nth SAR acquisition date by averaging $N - 1$ unwrapped interferograms that share the common reference SAR scene n as (Tymofyeyeva & Fialko, 2015; Zebker et al., 2023):

$$\bar{\alpha}_n = \frac{\lambda}{4\pi}\frac{1}{N-1}\left(\sum_{k=1,k\neq n}^{N}\phi_{k,n}\right) = \alpha_n + \frac{1}{N-1}\left(\sum_{k=1,k\neq n}^{N}\Delta d_{k,n} - \sum_{k=1,k\neq n}^{N}\alpha_k\right) \tag{5}$$

Because tropospheric turbulence noise can be considered as random in time with zero mean, the term $\frac{1}{N-1}\sum\alpha_k \to 0$ when N is sufficiently large (Emardson et al., 2003; Onn, 2006). Under the assumption that $\frac{1}{N-1}\sum\Delta d_{k,n}$ is relatively small compared to α_n, we compute $\bar{\alpha}_n$ at each pixel to obtain a tropospheric turbulence noise map $A^{(n)}$ for the nth SAR acquisition date over the entire study area. This assumption is reasonable for our algorithm design, because the goal of the algorithm is to enable accurate interpretation of InSAR results when surface deformation signals are relatively small compared to the tropospheric noise level in individual interferograms. In the case that a large deformation signal well above the noise level is present, Zebker et al. (2023) discussed methods that can better separate deformation signals and tropospheric noise, which is beyond the scope of this paper.

We next compute the 2D Power Spectral Density (PSD) of the nth tropospheric noise estimates at wavenumber k_x, k_y (with units $1/m$) as (Jacobs et al., 2017):

$$PSD_n(k_x, k_y) = \frac{|\widehat{A^{(n)}}|^2}{N_x N_y\left(\frac{1}{\Delta x \Delta y}\right)} \tag{6}$$

where $\widehat{A^{(n)}}$ is the Discrete Fourier transform (DFT) of the nth tropospheric noise map $A^{(n)}$, Δx and Δy are the interferogram pixel spacings (in meters) in the x and y directions, N_x and N_y are the total number of pixels in the x and y directions, and the squared absolute value and division are pixel-wise operations.
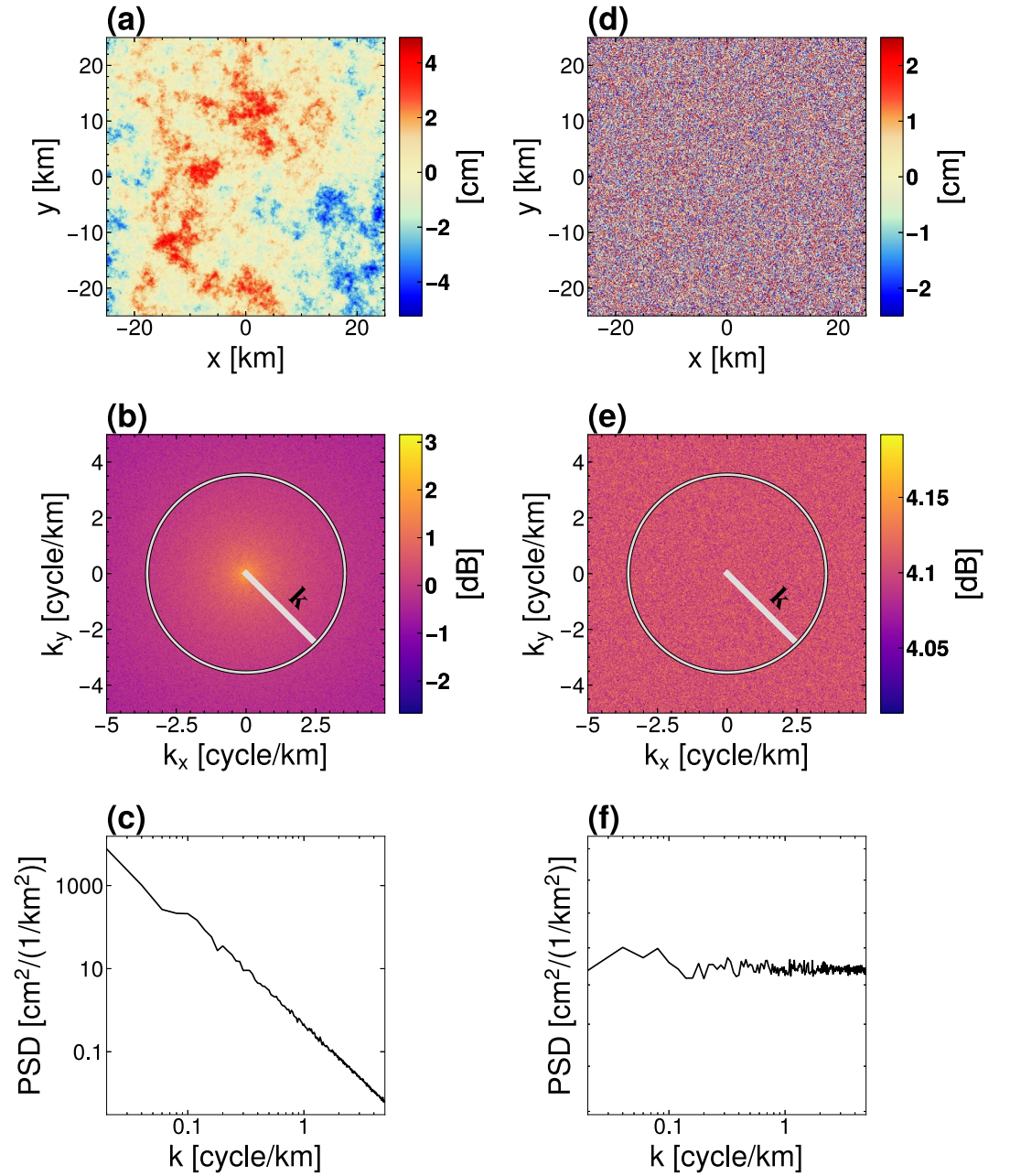
Figure 4. (a) A simulated 2D turbulent atmospheric noise map with 500×500 pixels at 100 m pixel spacing. (b) 2D Power Spectral Density (PSD) of the tropospheric noise map in panel (a). (c) 1D PSD as a function of wavenumber $k = \sqrt{k_x^2 + k_y^2}$, under the assumption that tropospheric noise is isotropic. (d) A simulated 2D white noise map (spatially uncorrelated) with the same dimension and pixel spacing as panel (a, e) 2D PSD of the white noise map in panel (d). (f) 1D PSD as a function of wavenumber $k = \sqrt{k_x^2 + k_y^2}$. Here we averaged the 1D PSD of 50 2D white noise instances to improve the statistical stability of the spectral estimates.

As an example, Figure 4a shows a synthetic 2D tropospheric turbulence noise map. We calculate the 2D PSD of the noise map following Equation 6 (Figure 4b). Under the assumption that tropospheric noise is isotropic, we average all pixels with a distance $k = \sqrt{k_x^2 + k_y^2}$ from the origin to generate a 1D PSD as a function of k (Hanssen, 2001). We plot the 1D PSD on a log-log scale, which rolls off following a power law at higher

frequencies (Figure 4c). By contrast, the power spectrum of spatially uncorrelated noise is relatively flat across all frequencies k (Figures 4d–4f).

2.4. Classification of Deformation and Noise Features

Based on the average 1D PSD of N InSAR-observed tropospheric turbulence noise maps, we can simulate N 2D noise instances $S^{(1)}, \ldots, S^{(N)}$ that closely resemble the real tropospheric noise over the study area (Hanssen, 2001). Using these simulated tropospheric noise maps, we form up to $N(N - 1)/2$ noise-only interferograms. We then use these synthetic interferograms as input to derive a synthetic surface deformation map following the same processing strategy for analyzing real InSAR observations. Because deformation signals are not present in the synthetic InSAR data set, all spatially coherent features detected in the synthetic surface deformation map are associated with the residual tropospheric noise. We record the radius r_k, the filter response magnitude $|g_k|$, and the magnitude $|\overline{d_k}|$ of each noise feature using our automatic feature detection algorithm.

We generate many synthetic signal-free surface deformation maps through repeated noise-only interferogram simulations, record the characteristics of all detected noise features, and create 2D histograms of the noise attributes (filter response magnitude vs. radius and feature magnitude vs. radius). These 2D histograms of the noise attributes are used to determine which candidate features detected in the real deformation map are likely due to tropospheric noise artifacts.

3. Test Sites and Case Study Descriptions

3.1. Synthetic Test Case

We first demonstrate our workflow on a synthetic test case. We used a PSD with a $-8/3$ power law slope to simulate 10 synthetic tropospheric turbulence noise images of size 800×800 and 100 m pixel spacing. From these 10 noise images, we formed 5 independent noise-only interferograms. We then averaged these 5 independent noise-only interferograms (known as stacking), and ran the feature detection algorithm on the result. We recorded the size, location, and magnitude of all detected features. We repeated this simulation process 500 times to estimate the turbulence noise probability density as a function of feature size (km) and feature magnitude (cm). To simulate a synthetic noisy deformation map, we added 10 deformation bowls, ranging from 0.5 to 3.5 cm in amplitude, to the average of five independent noise-only interferograms. We ran our feature detection algorithm on the noisy deformation map and recorded the size, the filter response magnitude, and the magnitude of each candidate feature. Finally, we quantified the uncertainty of these detections using the previously-computed 2D turbulence noise probability density function.

3.2. West Texas: Long-Term Cumulative Deformation

We further demonstrate the algorithm on a study site over an 80,000 km^2 oil-producing region in the Permian Basin, West Texas (Figure 5). We processed 84 ascending Sentinel-1 scenes (Path 78, Frames 94–104) acquired between November 2014 and January 2019 using a geocoded single look complex (SLC) processor (Zebker, 2017; Zheng & Zebker, 2017). We imposed no maximum spatial baseline and a maximum temporal baseline of 800 days for interferogram selection, resulting in 2,550 multi-looked interferograms with 120 m pixel spacing. We successfully unwrapped all interferograms using the Statistical-cost, Network-flow Algorithm for Phase Unwrapping (SNAPHU) algorithm (Chen & Zebker, 2001) due to the lack of vegetation and decorrelation artifacts. Because InSAR measures relative LOS deformation with respect to a reference point, we used the GPS station TXKM (Figure 5, yellow dot), with minimal surface deformation as the reference to calibrate InSAR results.

We employed a stacking approach to solve for surface deformation maps from Sentinel-1 interferograms (Sandwell & Price, 1998; Staniewicz et al., 2020). At a radar pixel of interest, we calculated the average LOS velocity v_{avg} over a time period of interest T as:

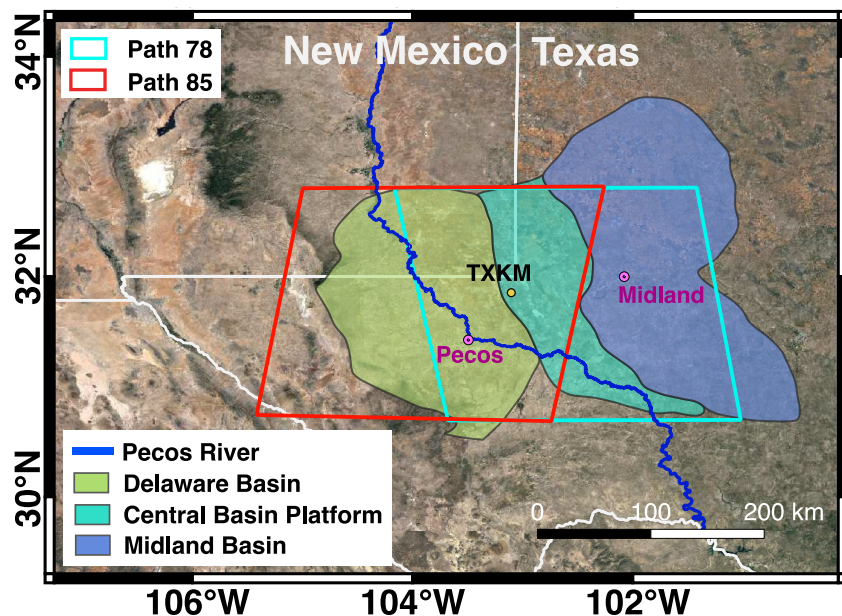$$v_{avg} = \frac{\sum_{i \in G} \Delta d_i}{\sum_{i \in G} t_i} \tag{7}$$

Figure 5. GPS and InSAR data coverage over the Permian Basin. Teal and red boxes indicate Sentinel-1 InSAR coverage for ascending Path 78 and descending Path 85. GPS station TXKM (yellow dot) was used as the reference point for both paths.

where G is a subset of interferograms formed using two SAR scenes acquired within the time period T. The LOS measurement (in cm) and the temporal baseline of the ith interferogram in G are written as Δd_i and t_i respectively. The total cumulative LOS deformation can be approximated as the average LOS velocity v_{avg} times the total time period T. In this study, we focused on the LOS cumulative deformation over three periods of interest: November 2014 to January 2017 (29 SAR acquisitions that span ~2 years), November 2014 to January 2018 (52 SAR acquisitions that span ~3 years), and November 2014 to January 2019 (84 SAR acquisitions that span ~4 years). As the number of SAR acquisitions increases, the residual tropospheric noise level decreases in the final surface deformation solutions. We note that the West Texas cumulative LOS deformation maps were validated using independent GPS observations with ~2 mm/year accuracy in our earlier study (Staniewicz et al., 2020). Here we used these three LOS maps as input to the automatic feature detection algorithm as described in Section 2.2. Alternatively, other InSAR processing algorithms (e.g., the Small Baseline Subset method or SBAS [Berardino et al., 2002]) may be employed to derive surface deformation maps as the algorithm input as well.

In the West Texas case, the dominant noise term is the tropospheric turbulence noise (Staniewicz et al., 2020). To determine the noise detection thresholds, we estimated the tropospheric turbulence noise for each SAR acquisition date using all interferograms that contain this SAR scene, known as common reference stacking (Tymofyeyeva & Fialko, 2015). We then removed a long-wavelength quadratic ramp in each noise map to focus on local deformation features, and calculated the average tropospheric noise spectrum (Section 2.3). We next generated a synthetic surface deformation map from simulated signal-free interferograms that follow the tropospheric noise spectrum derived from the real interferograms (Section 2.4). For the 2-year cumulative LOS deformation case (November 2014 to January 2017), we formed synthetic interferograms using 29 tropospheric noise instances randomly generated from the average 1D PSD. We ran our feature detection algorithm on the synthetic 2-year noise-only cumulative deformation map, and recorded the size, the filter response magnitude, and the magnitude of each detected noise feature. We repeated these simulations until the number of recorded noise features exceeded 100,000. We smoothed the resulting histograms using a kernel density estimate (KDE) (Scott, 2015), and generated 2D empirical PDFs of the residual tropospheric noise attributes. Based on these noise distributions, we removed features detected from the real 2-year cumulative deformation maps with more than 5% chance of being tropospheric noise. Similarly, we detected deformation features that are unlikely associated with tropospheric noise from the 3-year (52 Sentinel-1 acquisitions) and 4-year (84 Sentinel-1 acquisitions) cumulative LOS deformation maps.
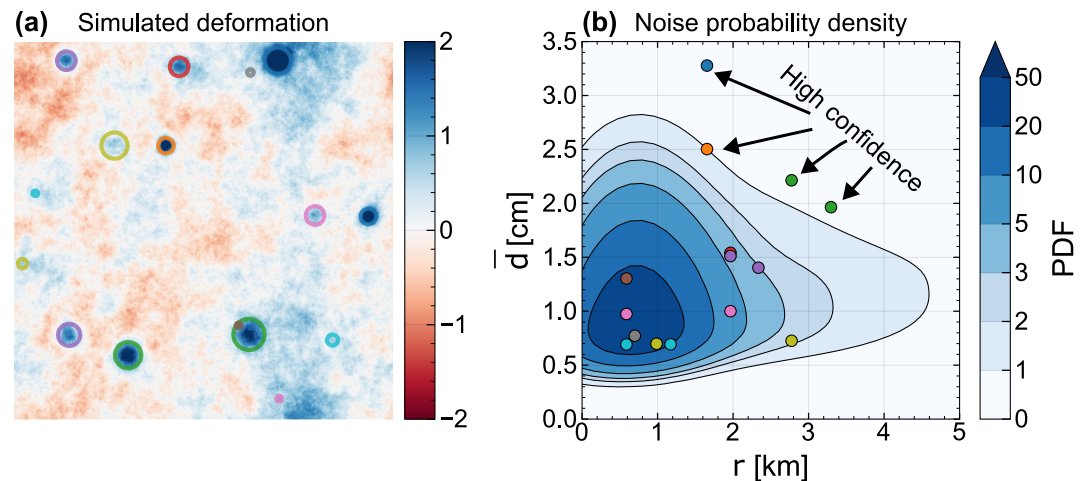
Figure 6. A synthetic test case. (a) A simulated field of 10 deformation bowls, with magnitudes ranging from 0.5 to 3.5 cm, superimposed on a synthetic noise field with peak-to-peak magnitude of 2.5 cm. Colored circles indicate locations of 14 detected candidate features. (b) The Probability Density Function (PDF) (PDF) of the detected noise features as a function of feature size (km) and feature magnitude (cm) for the synthetic case. Darker blue indicates regions of higher probability for detecting a noise feature. Four deformation features with the highest magnitudes all have very low chance of arising from residual tropospheric noise ($p < 0.05$).

As a comparison, we also processed 81 descending Sentinel-1 scenes (Path 85 Frames 483–493) acquired between November 2014 and January 2019 (Figure 5). The same GPS station, TXKM, was used as the reference location to calibrate all interferograms. Following the same processing strategy, we estimated three cumulative deformation maps spanning November 2014 to January 2017 January 2018, and January 2019. We characterized the tropospheric noise from InSAR data, and identified deformation features in the cumulative deformation maps that are likely real.

3.3. West Texas: Transient Deformation

To illustrate how our detection and uncertainty quantification workflow on a transient deformation signal, we also processed Sentinel-1 interferograms containing the coseismic deformation signal of the 26 March 2020 M_W 5.0 earthquake near Mentone, TX (Skoumal et al., 2020). First, using one coseismic interferogram from 2020/03/25 to 2020/04/04, we derived the 1D PSD of this interferogram and simulated interferograms that follow the same spectrum. We detected spatially coherent features from these simulated interferograms and produced the 2D PDF of the size and magnitude of the detected noise features. We then detected features in the coseismic interferogram and compared the results to the noise PDF.

We then averaged 7 coseismic interferograms which all contain the signal of interest. We followed Section 2.3 to estimate the tropospheric noise PSD of each of the 14 SAR acquisition date. We then generated seven noise-only synthetic interferograms using these PSDs, and recorded the size and magnitude of the detected features in the averaged synthetic interferogram. We repeated this process and generated the PDF of the tropospheric noise features from simulated 7-interferogram stacks. Finally, we assigned a confidence to all detections on the real earthquake deformation map.

4. Results and Discussion

4.1. Synthetic Test Results

Figure 6a shows all 14 detected candidate features in the synthetic test case, where 10 synthetic deformation features (with magnitudes ranging from 0.5 to 3.5 cm) are added to a random noise field with peak-to-peak magnitude of 2.5 cm. Given that many of the candidate features have a high probability of being from turbulence noise, we quantified the uncertainty by plotting the feature size r (km) and feature magnitude $|\bar{d}|$ (cm) against the estimated 2D turbulence noise probability density function (PDF). As shown in Figure 6b, the four
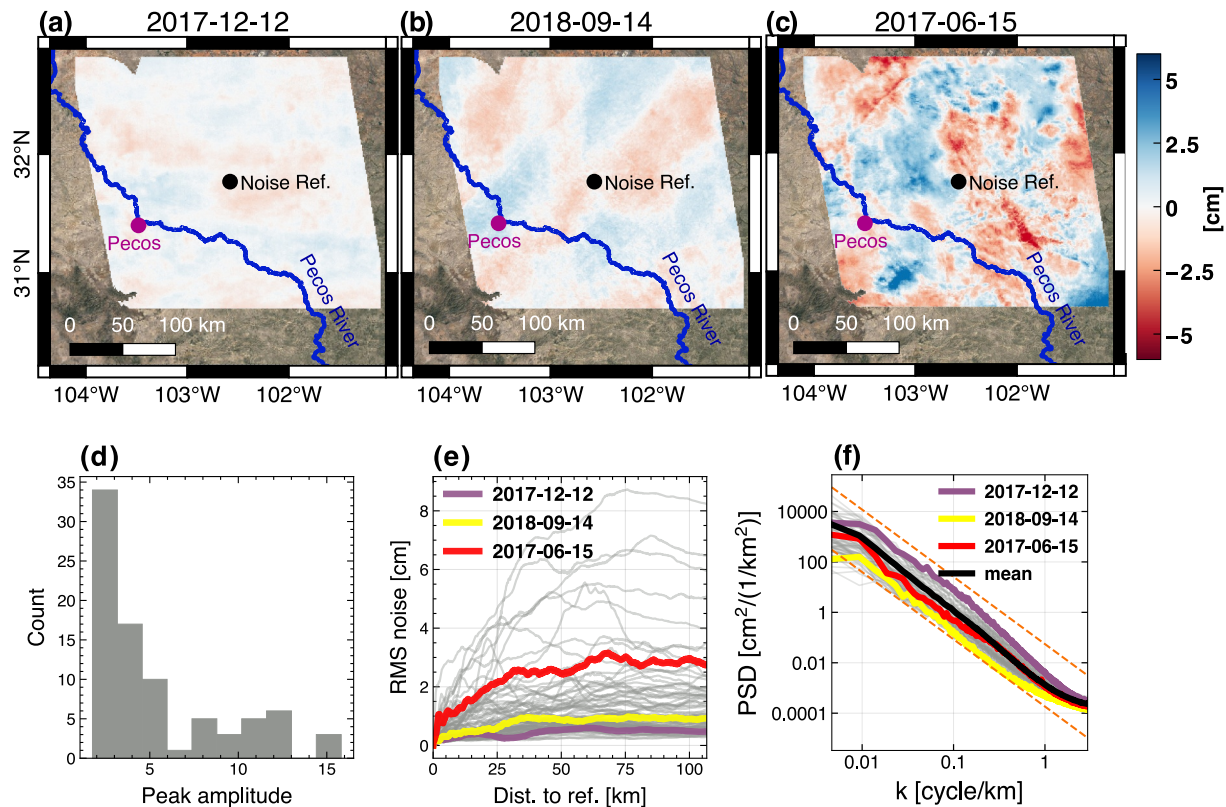
Figure 7. InSAR-estimated tropospheric turbulence noise maps along the LOS direction for three Path 78 SAR acquisitions: (a) 2017-12-12 (up to 1.8 cm noise), (b) 2018-09-14 (up to 3.2 cm noise), and (c) 2017-06-15 (up to 12.6 cm noise). (d) The distribution of the maximum tropospheric noise magnitude (in centimeters) observed in each of the 84 Sentinel-1 West Texas acquisitions from Path 78. (e) The root mean squared value of tropospheric noise versus distance from the reference point for 84 Sentinel-1 scenes from Path 78. (f) The estimated 1D PSDs for 84 Sentinel-1 scenes from Path 78. In panels (e, f), the color lines represent three SAR acquisitions (panels (a–c)) with different tropospheric noise levels. The black line in panel (f) represents the mean Power Spectral Density of all 84 acquisitions. The orange dotted lines show the $-8/3$ power law slope.

deformation features with the largest magnitudes all have very low probabilities of being noise ($p < 0.05$). Therefore, we labeled these as detected deformation features with high confidence.

4.2. Path 78 Detections

Figures 7a–7c shows three estimated tropospheric noise maps for Sentinel-1 ascending Path 78 acquisitions 2017-12-12, 2018-09-14, and 2017-06-15. We observe spatially coherent turbulence features ranging from a few kilometers up to tens of kilometers in diameter, and the magnitude of the tropospheric turbulence noise varies substantially on different days (Figure 7d). For example, the maximum absolute tropospheric noise observed on 2017-12-12, 2018-09-14, and 2017-06-15 are 1.8, 3.2, and 12.6 cm, respectively. Overall, ∼50% of Path 78 scenes were acquired in quiet atmospheric conditions with a maximum noise level under 4 cm. Approximately, 35% scenes were acquired in moderate turbulence conditions (a maximum noise level of 4–10 cm), and 15% scenes were acquired in strong turbulent noise conditions (a maximum noise level of 11–15 cm). Our results are consistent with existing tropospheric noise studies that tropospheric noise does not always follow a Gaussian distribution and may contain large outliers (Staniewicz et al., 2020; Zebker et al., 2023).

Because InSAR phases are measured with respect to a reference point, we calculated tropospheric noise estimates relative to the center of the map (the noise reference point). We plotted the mean absolute tropospheric noise versus distance to the noise reference point (Figure 7e). For the majority of the Path 78 acquisitions, tropospheric turbulent noise increases as the square root of the distance for the first ∼50 km, and then the magnitude of the tropospheric noise does not change much as the distance increases. This means that the tropospheric noise is spatially correlated with a correlation length of ∼50 km, and the tropospheric noise magnitude over the flat portion of the curve is a measure of the noise activity level. The 1D PSDs for the 84 tropospheric turbulence noise
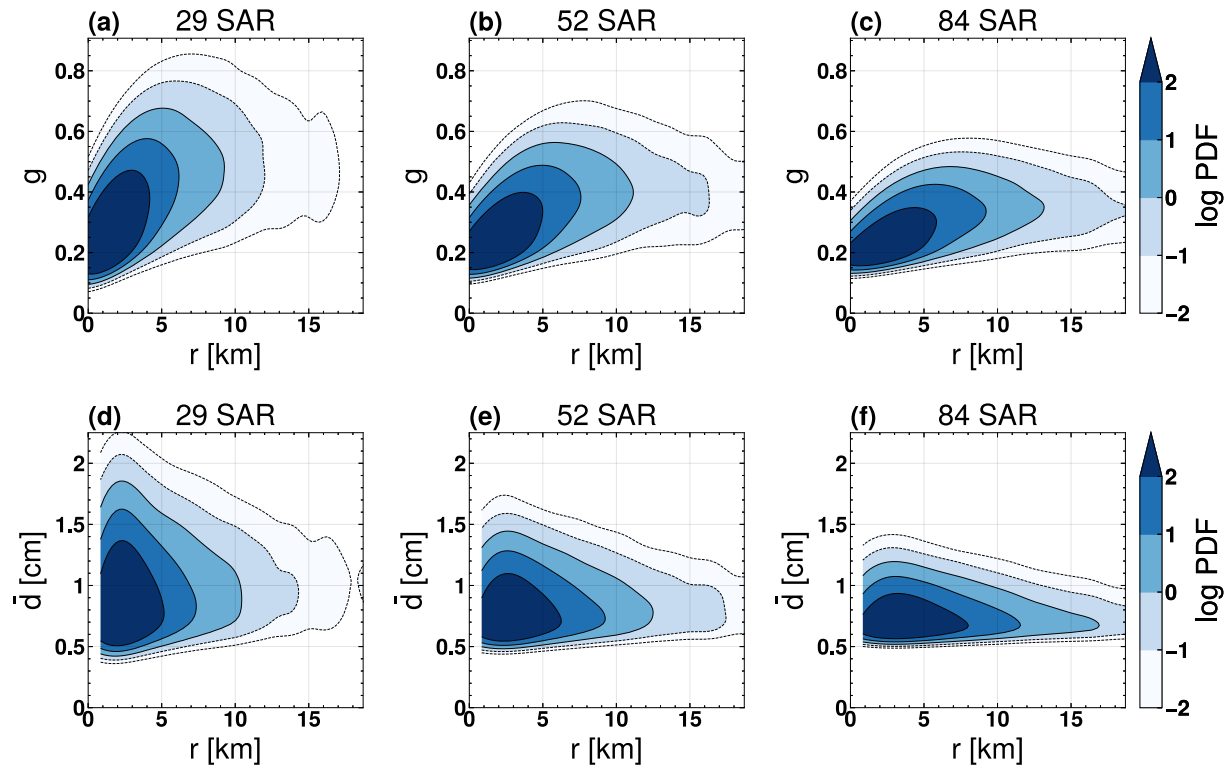
Figure 8. (a–c) Log Probability Density Function (PDF) (PDF) of detecting tropospheric noise features as a function of feature size r and filter response magnitude $|g|$ for three cumulative LOS deformation maps: November 2014–January 2017 (29 SAR scenes from Path 78), November 2014–January 2018 (52 SAR Scenes from Path 78), and November 2014–January 2019 (84 SAR Scenes from Path 78). (d–f) Log PDF (PDF) of detecting tropospheric noise features as a function of feature size r and feature magnitude $|d|$ for the same three cumulative LOS deformation maps. The PDFs were generated from 2D histograms using a kernel density estimate (Scott, 2015).

maps give an alternative view of the distribution of noise power over different frequencies (Figure 7f). For most spatial frequencies, the PSDs decay with approximately the $-8/3$ power law slope (dotted orange lines) described in Hanssen (2001). This slope flattens at the low frequencies because we removed the quadratic phase in the noise solutions. The slope also flattens at high frequencies, where decorrelation noise introduces pixel-level variations in the noise map.

We applied the automatic feature detection algorithm to three Path 78 LOS cumulative deformation maps over three different periods of time: November 2014 to January 2017 (29 SAR acquisitions that span ~2 years), November 2014 to January 2018 (52 SAR acquisitions that span ~3 years), and November 2014 to January 2019 (84 SAR acquisitions that span ~4 years). By imposing the prior knowledge that oil- and gas-production-related deformation bowls are unlikely to be larger than 30–40 km in the Permian Basin (Staniewicz et al., 2020), the maximum detected feature radius r was set to 20 km. We also applied the feature detection algorithm to the synthetic noise-only surface deformation maps, and recorded the statistics of the tropospheric noise features for the 2-year, 3-year, and 4-year cases, respectively (Figure 8). We found that most tropospheric turbulence noise features have small radii ($r < 5$ km). For the 29 SAR acquisition (~2-year) case, the noise features are unlikely to be larger than 2 cm in magnitude or have a filter response stronger than 0.7. For the 52 SAR acquisition case (~3-year), the noise features are unlikely to be larger than 1.5 cm in magnitude or have a filter response stronger than 0.6. For the 84 SAR acquisition case (~4-year), the noise features are unlikely to be larger than 1.2 cm in magnitude or have a filter response stronger than 0.5. This agrees with the InSAR deformation mapping uncertainty estimated based on independent GPS validation for the same path 78 Sentinel-1 data set (Staniewicz et al., 2020). Using the empirical PDFs of the noise attributes, we removed detections with more than 5% chance of being noise from three Path 78 cumulative deformation maps (Figure 9). We identified 57 deformation features in the Nov. 2014–Jan. 2017 cumulative deformation map, 147 features in the Nov. 2014–Jan. 2018 map, and 268 features in the Nov. 2014–Jan. 2019 map. The increasing number of detected deformation features is consistent with the sharp rise in the rate of oil and gas production over the study period (Figure S2 in Supporting
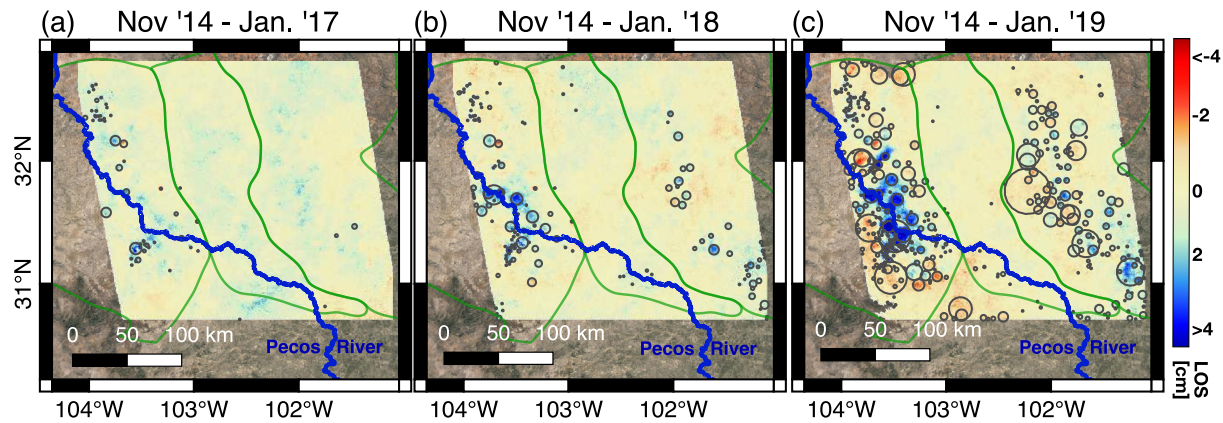
Figure 9. Detected deformation features (gray circles) from the three Path 78 cumulative LOS deformation maps. Features with more than 5% chance of being noise have been removed. Green lines correspond to the boundaries of the Delaware Basin, Central Basin Platform, and Midland Basin from west to east.

Information S1), as well as the reduced noise level in the InSAR cumulative deformation solutions resulting from a larger number of SAR acquisitions. The detected features are mainly clustered in regions within the Midland Basin and the Delaware Basin, which are spatially correlated with oil production and wastewater injection activities (Hennings et al., 2023). In the Southern Delaware Basin, the observed linear deformation features parallel the inferred favorable fault plane orientation proposed by Lund Snee and Zoback (2018), and they align with a cluster of recent shallow earthquakes cataloged by TexNet (Savvaidis et al., 2019). Very few deformation features were detected in the Central Basin Platform, where oil and gas are mostly produced from conventional reservoirs and the subsurface pressure was well maintained.

We note that real deformation signals may leak into individual noise estimates derived from the common reference stacking approach. To demonstrate the effect of imperfect tropospheric noise estimates, Figure 10a shows the tropospheric noise estimates on a typical date (2018-09-04), and Figure 10b shows the cumulative linear LOS deformation solution over the entire study period (from Nov. 2014 to Jan. 2019; the deformation signals in most individual interferograms are much smaller). The estimated 1D PSDs for the noise-only map and the noise plus deformation map are very similar (Figure 10c), and thus the simulated interferograms derived from these two PSDs follow similar spectra. This is because the observed phases in individual West Texas Sentinel-1 interferograms are mostly associated with up to ±15 cm tropospheric turbulence noise, and the expected deformation signal magnitude ($\sim$a few millimeters to centimeter per year) is much smaller. We conclude that the presence of millimeter-to-centimeter level deformation signals does not lead to noticeable errors in tropospheric noise spectrum estimates, nor the simulated noise maps, for our West Texas case.

4.3. Path 85 Detections

Similar to the ascending Path 78 results, approximately 50% of descending Path 85 scenes were acquired in quiet atmospheric conditions with a maximum noise level under 4 cm (Figure 11a). However, only 2 out of 81 descending scenes were acquired in strong turbulent noise conditions (a maximum noise level over 10 cm), while
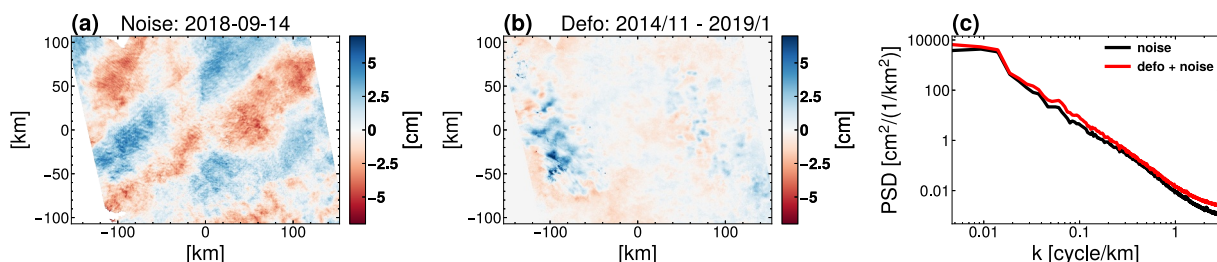

Figure 10. (a) InSAR-estimated tropospheric noise map along the LOS direction for the Path 78 SAR acquisition 2018-09-14. (b) Cumulative LOS deformation from Nov. 2014 to Jan. 2019 as inferred from Sentinel-1 Path 78 InSAR data. (c) 1D PSDs derived from the tropospheric noise map (black) and the tropospheric noise plus deformation map (red).
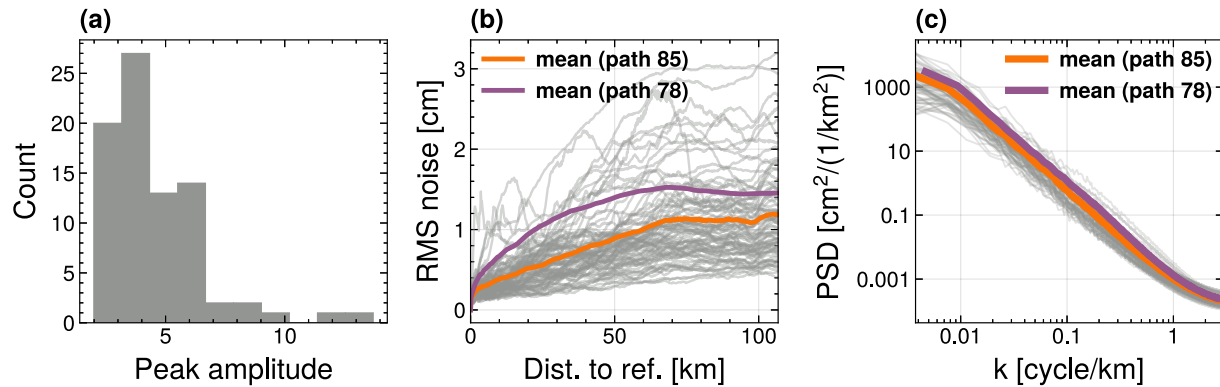
Figure 11. (a) The distribution of peak tropospheric noise magnitude (in centimeters), (b) the root mean squared value of tropospheric noise versus distance from the center of the map, and (c) the estimated 1D PSDs for 81 Sentinel-1 Path 85 acquisitions used in this study. In panels (b, c), the color lines represent the average estimates for Path 85 (orange) and Path 78 (purple).

14 out of the 84 ascending scenes were acquired in such conditions. We also found that the average tropospheric noise level is lower for Path 85 than Path 78 (Figures 11b–11c). For example, the mean absolute tropospheric noise is 50% larger for Path 78 than Path 85 at 50 km, and the mean noise power density is more than 2 times larger for Path 78 than Path 85 at a spatial frequency of 0.1 cycles/km. We summarized the noise statistics of Path 78 and Path 85 acquisitions in Table 1. Our tropospheric noise estimates for ascending and descending paths are consistent with the fact that Sentinel-1 satellites acquire Path 78 data over West Texas at 7:50 p.m. local time, and Path 85 data at 6:55 a.m. local time. The expected tropospheric noise signatures are typically more substantial in late afternoon than early morning.

Our algorithm identified similar numbers of spatially coherent features from the ascending and descending cumulative LOS deformation maps that span the same period of interest (Figure 12). Because the tropospheric noise level is generally lower in Path 85 data, fewer Path 85 detections need to be removed because they have more than 5% chance of being tropospheric noise. As a result, we detected more deformation features from the Path 85 data set than from the Path 78 data set. The number of detected deformations from both paths increases substantially over the study period, which follows the significant rise in oil production within the Permian Basin due to advances in shale recovery technologies (Figure S2 in Supporting Information S1). It is also worth noting that the InSAR cumulative LOS deformation maps from both paths were validated using independent GPS observations (Staniewicz et al., 2020). The Path 78 and Path 85 maps appear different. This is because (a) the ascending and descending LOS unit vectors are different; and (b) non-negligible eastward deformation signals are present in the Delaware Basin, which contribute to the ascending and descending LOS deformation in different ways.

4.4. Transient Deformation Detection

Figure 13a shows a 30 km-by-30 km Sentinel-1 interferogram (2020/03/25–2020/04/04; Path 85) that contains the Mentone earthquake coseismic deformation signal. Despite the small study area, the 2D PDF shows that the magnitude of tropospheric noise features regularly reached 1 cm (Figure 13b). We applied the automatic feature detection algorithm to the co-seismic interferogram shown in Figure 13a, which detected the coseismic deformation feature and several of the stronger tropospheric noise features. Although the algorithm detected the real deformation feature (green circle), we only computed a moderate confidence level ($p = 0.06$) that this feature was not a turbulence artifact. Similar magnitude atmospheric artifacts (confidence $p = 0.08, 0.11$) are also detected in the interferogram.

After averaging more interferograms that span the same earthquake, the noise level is reduced and the confidence of detection substantially increases. Using 7 interferograms formed from 14 SAR acquisitions (7 before and 7 after the earthquake), the resulting coseismic deformation map contains considerably fewer visual tropospheric noise artifacts (Figure 13c). Correspondingly, the estimated PDF of tropospheric noise features shows lower probability for

Table 1
Tropospheric Noise Characteristics for Sentinel-1 Path 85 and Path 78 Data Over West Texas

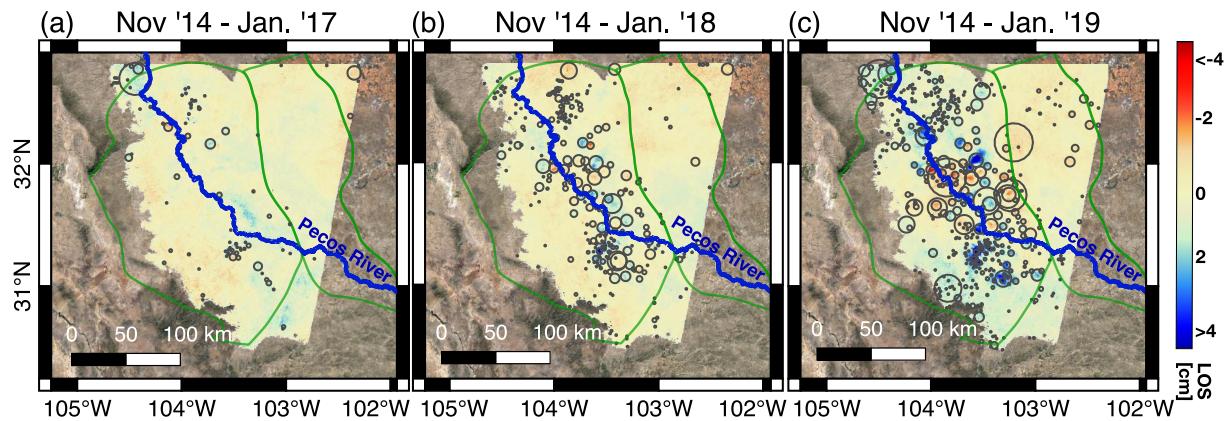|	Path 78	Path 85
Average Variance [cm^2]	1.38	0.78
Variance of the Noisiest Date [cm^2]	10.68	3.74
Average Peak Amplitude [cm]	5.36	4.58
Peak Amplitude of the Noisiest Date [cm]	15.81	13.72

Figure 12. Detected deformation features (gray circles) from the three Path 85 cumulative LOS deformation maps. Features with more than 5% chance of being noise for their radius have been removed. Green lines illustrate the boundaries of the Delaware Basin and Central Basin Platform, from west to east.
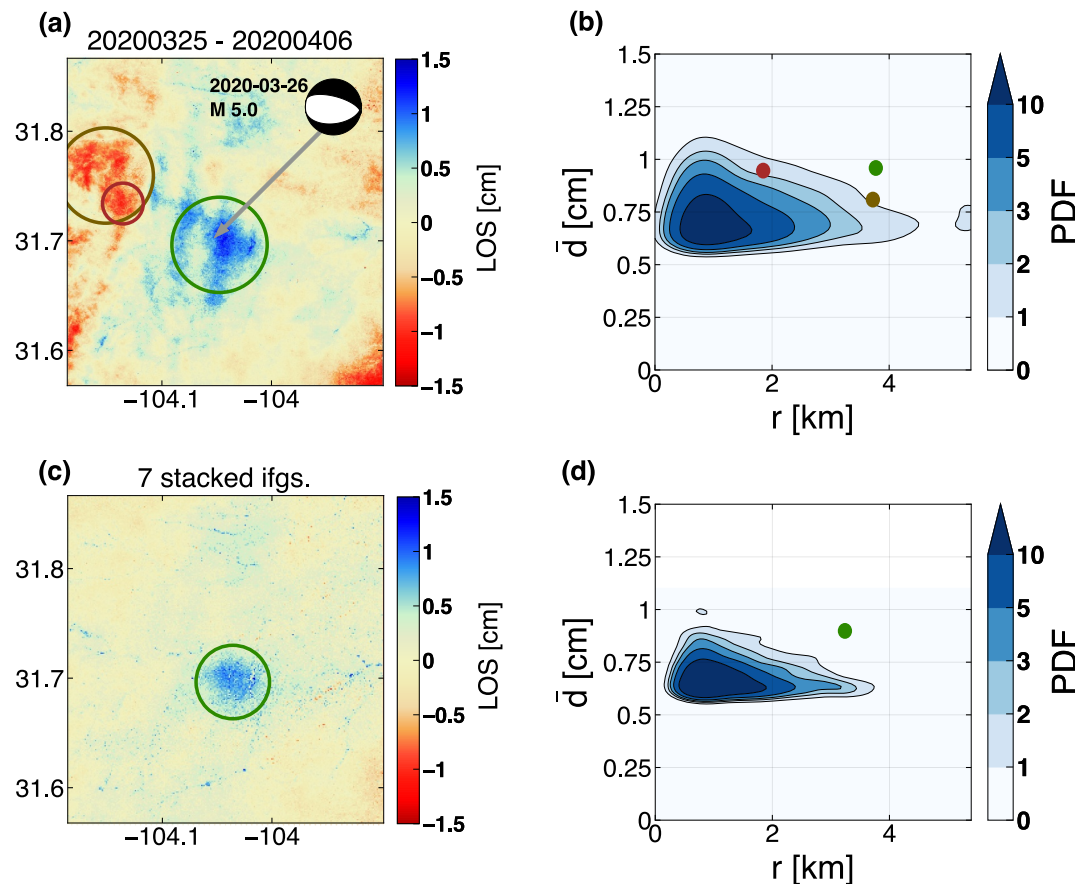

Figure 13. (a) A coseismic interferogram (2020/03/25–2020/04/06) that spans the 26 March 2020 Mentone earthquake, Texas. Color circles indicate the top 3 detected features. The focal mechanism plot was derived by USGS National Earthquake Information Center. (b) Probability Density Function (PDF) (PDF) of the detected noise features from simulated interferograms as a function of feature size (km) and feature magnitude (cm) for the single interferogram case. Color dots show the three detected features in panel (a). (c) Estimated coseismic LOS deformation as derived from averaging 7 interferograms that span the March 26 event. The green circle shows the one detected feature with very high likelihood of being real ($p < 0.001$). (d) PDF of the detected noise features from simulated interferograms as a function of feature size (km) and feature magnitude (cm) for the 7-interferogram stacking case. The green dot indicates the detected feature in panel (c).

~1 cm features (Figure 13d). When we applied the automatic feature detection algorithm to this improved deformation map in Figure 13c, we detected one deformation feature with very high confidence ($p < 0.001$). This feature matches the deformation pattern previously reported by Skoumal et al. (2020). This example demonstrates how our algorithm accurately represents uncertainty in scenarios with limited data (single interferogram), while also capturing the improved confidence that comes from reducing tropospheric noise through stacking multiple interferograms.

4.5. Detection Threshold Analysis for Path 78 and Path 85 Noise Levels

We performed synthetic tests designed to quantify our algorithm's sensitivity, precision, and robustness. We assessed performance on cumulative deformation mapping by simulating synthetic deformation signals and adding realistic noise derived from estimated tropospheric noise levels for both ascending (Path 78) and descending (Path 85) data sets.

We simulated tropospheric noise maps based on the Path 78 PSDs (Figure 7f), matching the number of dates used in our real 4-year cumulative LOS deformation analysis (November 2014–January 2019). We generated cumulative deformation maps by stacking the synthetic noise interferograms and superimposing 20 randomly placed deformation bowls with radii ranging from 2 to 7 km at fixed amplitudes. We applied our detection algorithm to the noisy synthetic deformation maps and used the turbulence noise PDFs (Figure 8) to compute a probability that the detections were noise artifacts. We recorded true detections, false positives, and missed detections to find performance metrics. We repeated this simulation using deformation amplitudes ranging from 0.5 to 3 cm in increments of 0.25 cm.

The synthetic test shows that our algorithm reliably detects deformation with amplitudes $1-1.5$ cm under noise conditions similar to the Path 78 data set (Figure S3 in Supporting Information S1). We calculated the precision (the fraction of detected features that are true deformation signals), recall (the fraction of true signals successfully detected), and the F_1 score (the harmonic mean of precision and recall) of our algorithm at each simulated deformation level. The precision exceeds 0.8 for all amplitudes of 1.25 cm or greater (Figure S3e in Supporting Information S1). Both recall and F_1 score approach 0.9 at ~1.5 cm (Figures S3f and S3g in Supporting Information S1). Testing a p-value threshold of 0.001, 0.01, and 0.05 (Figure S3 in Supporting Information S1, colored lines), showed that the precision and recall metrics are relatively insensitive to the choice of threshold.

We performed the same analysis on the Path 85 cumulative 4-year data set (Figure S4 in Supporting Information S1). Since the noise power is smaller for this descending data set (Figure 11), the confidence of the detections rises more quickly as our simulated deformation signals increase in amplitude. For example, the recall (Figure S4b in Supporting Information S1) reaches above 0.95 for signals 1.5 cm an larger, compared to a recall of approximately 0.8 under the noisier conditions of Path 78.

4.6. Temporal and Spatial Stationarity of Tropospheric Noise

Previous studies have investigated the seasonal amplitude variations of tropospheric noise in InSAR (Fattahi & Amelung, 2015). In our West Texas InSAR analyses, we included a similar number of acquisitions from each season to mitigate bias resulting from sampling irregularities. Although the PSDs shown in Figure 7f exhibit variations in power between different seasons, we observed minimal differences in the final noise PDFs when simulating noise maps using individual PSDs or the average PSD. When the temporal sampling rate is irregular, simulating tropospheric noise from seasonally-matching PSDs can lead to more accurate uncertainty quantification results.

Under the assumption of a second-order stationary random field, tropospheric turbulence noise can be fully described by its PSD representation (Chiles & Delfiner, 2012). This turbulence noise is isotropic when it follows the 3D Kolmogorov turbulence model (Hanssen, 2001). In this case, second-order stationarity in space is reasonable due to the deramping step performed on unwrapped interferograms. Although atmospheric noise may contain other anisotropic components in addition to the turbulence component of tropospheric noise (e.g., weather fronts moving in a specific direction based on the region's topography), these anisotropic weather effects do not typically produce artifacts similar to real deformation features in the final surface deformation map. The radially-averaged PSD used in this study provides a good approximation of the tropospheric turbulence noise that shares spatial characteristics similar to deformation features (Hanssen, 2001).

5. Conclusion

In this study, we introduced a computer vision algorithm to automatically detect spatially coherent deformation features from InSAR surface deformation maps and quantify the likelihood that these detections arise from tropospheric turbulence noise. The detection algorithm identifies deformation features of various sizes and amplitudes without relying on labeled training data. To robustly quantify uncertainty of noise artifacts, we characterized the turbulent tropospheric noise component directly from the InSAR data by estimating its PSD and generating synthetic noise samples. This allowed us to empirically assess detection reliability without requiring additional data or model for tropospheric noise characterization.

Our synthetic tests show high precision and recall for identifying deformation signals larger than ∼1.5 cm. We applied the method to the InSAR cumulative deformation maps over the Permian Basin from late 2014 to 2019, confidently detecting localized deformation associated with increased oil and gas production. Additionally, we demonstrated the algorithm's uncertainty quantification capabilities on single interferograms containing small, transient deformation signals. Our technique can be readily integrated with existing InSAR time series methods, facilitating large-scale deformation analyses of local deformation signals and comprehensive uncertainty quantification.

We emphasize that our InSAR-based deformation detection method is based on the assumption that random tropospheric turbulence noise is the dominant noise term. Outside the flat, arid Permian Basin, the dominant noise source may differ. In densely vegetated regions or areas with seasonal snow, decorrelation noise and phase-unwrapping errors can be non-negligible, so a more realistic uncertainty model could be obtained by incorporating the full coherence history (Zwieback & Meyer, 2022) or by using ensemble-processing strategies (Olsen et al., 2023). These extensions are additive, and may be combined with the computer-vision processing framework presented here.

Data Availability Statement

The software package for simulating tropospheric turbulence noise is available on Zenodo at Staniewicz (2025b). The package for estimating atmospheric noise and detecting deformation features is available at Zenodo at Staniewicz (2025a). Sentinel-1 single-look complex (SLC) images can be accessed from the Alaska Satellite Facility (ASF) DAAC. Processed InSAR deformation maps for West Texas from Staniewicz et al. (2020) used in this study are available at the Texas Data Repository at Staniewicz and Chen (2020).

References

Anantrasirichai, N., Biggs, J., Albino, F., Hill, P., & Bull, D. (2018). Application of machine learning to classification of volcanic deformation in routinely generated InSAR data. *Journal of Geophysical Research: Solid Earth*, *123*(8), 6592–6606. https://doi.org/10.1029/2018jb015911

Barnhart, W. D., & Lohman, R. B. (2013). Characterizing and estimating noise in InSAR and InSAR time series with MODIS. *Geochemistry, Geophysics, Geosystems*, *14*(10), 4121–4132. https://doi.org/10.1002/ggge.20258

Bekaert, D., Walters, R., Wright, T., Hooper, A., & Parker, D. (2015). Statistical comparison of InSAR tropospheric correction techniques. *Remote Sensing of Environment*, *170*, 40–47. https://doi.org/10.1016/j.rse.2015.08.035

Berardino, P., Fornaro, G., Lanari, R., & Sansosti, E. (2002). A new algorithm for surface deformation monitoring based on small baseline differential SAR interferograms. *Geoscience and Remote Sensing, IEEE Transactions on*, *40*(11), 2375–2383. https://doi.org/10.1109/TGRS.2002.803792

Cao, Y., Jónsson, S., & Li, Z. (2021). Advanced InSAR tropospheric corrections from global atmospheric models that incorporate spatial stochastic properties of the troposphere. *Journal of Geophysical Research: Solid Earth*, *126*(5). https://doi.org/10.1029/2020jb020952

Chaussard, E., Bürgmann, R., Shirzaei, M., Fielding, E. J., & Baker, B. (2014). Predictability of hydraulic head changes and characterization of aquifer-system and fault properties from InSAR-derived ground deformation. *Journal of Geophysical Research: Solid Earth*, *119*(8), 6572–6590. https://doi.org/10.1002/2014jb011266

Chen, C. W., & Zebker, H. A. (2001). Two-dimensional phase unwrapping with use of statistical models for cost functions in nonlinear optimization. *Journal of the Optical Society of America A*, *18*(2), 338–351. https://doi.org/10.1364/JOSAA.18.000338

Chen, J., Knight, R., Zebker, H. A., & Schreüder, W. A. (2016). Confined aquifer head measurements and storage properties in the San Luis Valley, Colorado, from spaceborne InSAR observations. *Water Resources Research*, *52*(5), 3623–3636. https://doi.org/10.1002/2015wr018466

Chen, J., Zebker, H. A., & Knight, R. (2015). A persistent scatterer interpolation for retrieving accurate ground deformation over InSAR-decorrelated agricultural fields. *Geophysical Research Letters*, *42*(21), 9294–9301. https://doi.org/10.1002/2015GL065031

Chen, J., Zebker, H. A., Segall, P., & Miklius, A. (2014). The 2010 slow slip event and secular motion at Kʻīlauea, Hawaiʻi, inferred from TerraSAR-X InSAR data. *Journal of Geophysical Research: Solid Earth*, *119*(8), 6667–6683. https://doi.org/10.1002/2014jb011156

Chiles, J.-P., & Delfiner, P. (2012). *Geostatistics: Modeling spatial uncertainty* (2nd ed. ed.). Wiley.

Efron, B., & Tibshirani, R. J. (1994). *An introduction to the bootstrap*. CRC Press.

Emardson, T. R., Simons, M., & Webb, F. H. (2003). Neutral atmospheric delay in interferometric synthetic aperture radar applications: Statistical description and mitigation. *Journal of Geophysical Research*, *108*(B5), 1–8. https://doi.org/10.1029/2002JB001781

Fattahi, H., & Amelung, F. (2015). InSAR bias and uncertainty due to the systematic and stochastic tropospheric delay. *Journal of Geophysical Research: Solid Earth*, *120*(12), 8758–8773. https://doi.org/10.1002/2015JB012419

Ferretti, A., Prati, C., & Rocca, F. (2000). Nonlinear subsidence rate estimation using permanent scatterers in differential SAR interferometry. *IEEE Transactions on Geoscience and Remote Sensing*, *38*(5), 2202–2212. https://doi.org/10.1109/36.868878

Hanssen, R. (2001). *Radar interferometry: Data interpretation and error analysis*. Springer.

Havazli, E., & Wdowinski, S. (2021). Detection threshold estimates for InSAR time series: A simulation of tropospheric delay approach. *Sensors*, *21*(4), 1124. https://doi.org/10.3390/s21041124

Hennings, P., Staniewicz, S., Smye, K., Chen, J., Horne, E., Nicot, J.-P., et al. (2023). Development of complex patterns of anthropogenic uplift and subsidence in the Delaware basin of west Texas and southeast New Mexico, USA. *Science of the Total Environment*, *903*, 166367. https://doi.org/10.1016/j.scitotenv.2023.166367

Hooper, A., Bekaert, D., Spaans, K., & Arıkan, M. (2012). Recent advances in SAR interferometry time series analysis for measuring crustal deformation. *Tectonophysics*, *514*, 1–13. https://doi.org/10.1016/j.tecto.2011.10.013

Hooper, A., Zebker, H., Segall, P., & Kampes, B. (2004). A new method for measuring deformation on volcanoes and other natural terrains using InSAR persistent scatterers. *Geophysical Research Letters*, *31*(23). Retrieved from https://doi.org/10.1029/2004GL021737

Huang, S. A., & Zebker, H. A. (2022). InSAR time-series analysis with a non-Gaussian detector for persistent scatterers. *Ieee Journal of Selected Topics in Applied Earth Observations and Remote Sensing*, *15*, 9208–9225. https://doi.org/10.1109/JSTARS.2022.3216964

Jacobs, T. D. B., Junge, T., & Pastewka, L. (2017). Quantitative characterization of surface topography using spectral analysis. *Surface Topography: Metrology and Properties*, *5*(1), 013001. https://doi.org/10.1088/2051-672x/aa51f8

Jolivet, R., Agram, P. S., Lin, N. Y., Simons, M., Doin, M.-P., Peltzer, G., & Li, Z. (2014). Improving InSAR geodesy using global atmospheric models. *Journal of Geophysical Research: Solid Earth*, *119*(3), 2324–2341. https://doi.org/10.1002/2013jb010588

Li, Z., Cao, Y., Wei, J., Duan, M., Wu, L., Hou, J., & Zhu, J. (2019). Time-series InSAR ground deformation monitoring: Atmospheric delay modeling and estimating. *Earth-Science Reviews*, *192*, 258–284. https://doi.org/10.1016/j.earscirev.2019.03.008

Lindeberg, T. (1993). Detecting salient blob-like image structures and their scales with a scale-space primal sketch: A method for focus-of-attention. *International Journal of Computer Vision*, *11*(3), 283–318. https://doi.org/10.1007/BF01469346

Lindeberg, T. (1998). Feature detection with automatic scale selection. *International Journal of Computer Vision*, *30*(2), 79–116. https://doi.org/10.1023/A:1008045108935

Liu, J., Hu, J., Bürgmann, R., Li, Z., & Jónsson, S. (2024). Mitigating atmospheric delays in InSAR time series: The DetrendInSAR method and its validation. *Journal of Geophysical Research: Solid Earth*, *129*(5), e2024JB028920. https://doi.org/10.1029/2024JB028920

Lohman, R. B., & Simons, M. (2005). Some thoughts on the use of InSAR data to constrain models of surface deformation: Noise structure and data downsampling. *Geochemistry, Geophysics, Geosystems*, *6*(1). https://doi.org/10.1029/2004gc000841

Lowe, D. G. (2004). Distinctive image features from scale-invariant keypoints. *International Journal of Computer Vision*, *60*(2), 91–110. https://doi.org/10.1023/B:VISI.0000029664.99615.94

Lund Snee, J., & Zoback, M. (2018). State of stress in the Permian basin, Texas and New Mexico: Implications for induced seismicity. *The Leading Edge*, *37*(2), 127–134. https://doi.org/10.1190/tle37020127.1

Olsen, K. M., Calef, M. T., & Agram, P. S. (2023). Contextual uncertainty assessments for InSAR-based deformation retrieval using an ensemble approach. *Remote Sensing of Environment*, *287*, 113456. https://doi.org/10.1016/j.rse.2023.113456

Onn, F. (2006). *Modeling water vapor using GPS with application to mitigating InSAR atmospheric distortions (Unpublished doctoral dissertation)*. Stanford University.

Parker, A. L., Biggs, J., Walters, R. J., Ebmeier, S. K., Wright, T. J., Teanby, N. A., & Lu, Z. (2015). Systematic assessment of atmospheric uncertainties for InSAR data at volcanic arcs using large-scale atmospheric models: Application to the cascade volcanoes, United States. *Remote Sensing of Environment*, *170*, 102–114. https://doi.org/10.1016/j.rse.2015.09.003

Pritchard, M. E., & Simons, M. (2004). An InSAR-based survey of volcanic deformation in the central Andes. *Geochemistry, Geophysics, Geosystems*, *5*(2). https://doi.org/10.1029/2003gc000610

Raspini, F., Bianchini, S., Ciampalini, A., Soldato, M. D., Solari, L., Novali, F., et al. (2018). Continuous, semi-automatic monitoring of ground deformation using sentinel-1 satellites. *Scientific Reports*, *8*(1), 7253. https://doi.org/10.1038/s41598-018-25369-w

Rouet-Leduc, B., Jolivet, R., Dalaison, M., Johnson, P. A., & Hulbert, C. (2021). Autonomous extraction of millimeter-scale deformation in InSAR time series using deep learning. *Nature Communications*, *12*(1), 6480. https://doi.org/10.1038/s41467-021-26254-3

Sandwell, D. T., & Price, E. J. (1998). Phase gradient approach to stacking interferograms. *Journal of Geophysical Research*, *103*(B12), 30183–30204. https://doi.org/10.1029/1998JB900008

Savvaidis, A., Young, B., Huang, G.-c. D., & Lomax, A. (2019). Texnet: A statewide seismological network in Texas. *Seismological Research Letters*. https://doi.org/10.1785/0220180350

Scott, D. W. (2015). *Multivariate density estimation: Theory, practice, and visualization* (2nd ed.). John Wiley and Sons. https://doi.org/10.1002/9781118575574

Segall, P. (2010). *Earthquake and volcano deformation*. Princeton University Press. Retrieved from https://books.google.com/books?id=x6Fp4hMBTpYC

Shanker, P., & Zebker, H. (2007). Persistent scatterer selection using maximum likelihood estimation. *Geophysical Research Letters*, *34*(22). Retrieved from https://doi.org/10.1029/2007GL030806

Skoumal, R. J., Kaven, J. O., Barbour, A. J., Wicks, C., Brudzinski, M. R., Cochran, E. S., & Rubinstein, J. L. (2020). The induced Mw 5.0 March 2020 West Texas seismic sequence. *Journal of Geophysical Research: Solid Earth*, *126*(1). https://doi.org/10.1029/2020jb020693

Staniewicz, S. (2025a). Scottstanie/blobsar: V0.1.0 [Software]. *Zenodo*. https://doi.org/10.5281/zenodo.15092867

Staniewicz, S. (2025b). Scottstanie/troposim: V0.2.0 [Software]. *Zenodo*. https://doi.org/10.5281/zenodo.15092869

Staniewicz, S., & Chen, J. (2020). Sentinel-1 InSAR surface deformation data over the Permian Basin [Dataset]. *Texas Data Repository*. https://doi.org/10.18738/T8/AVDBOJ

Staniewicz, S., Chen, J., Lee, H., Olson, J., Savvaidis, A., Reedy, R., et al. (2020). InSAR reveals complex surface deformation patterns over an 80,000km^2 oil-producing region in the Permian basin. *Geophysical Research Letters*, *47*(21), e2020GL090151. https://doi.org/10.1029/2020gl090151

Szeliski, R. (2022). *Computer vision: Algorithms and applications* (2nd ed.). Springer International Publishing. Retrieved from https://www.ebook.de/de/product/37918979/richard_szeliski_computer_vision.html

Tymofyeyeva, E., & Fialko, Y. (2015). Mitigation of atmospheric phase delays in InSAR data, with application to the eastern California shear zone. *Journal of Geophysical Research: Solid Earth*, *120*(8), 5952–5963. https://doi.org/10.1002/2015jb011886

Wang, K., & Chen, J. (2022). Accurate persistent scatterer identification based on phase similarity of radar pixels. *IEEE Transactions on Geoscience and Remote Sensing*, *60*, 1–13. https://doi.org/10.1109/TGRS.2022.3210868

Wang, Y., Dong, J., Zhang, L., Zhang, L., Deng, S., Zhang, G., et al. (2022). Refined InSAR tropospheric delay correction for wide-area landslide identification and monitoring. *Remote Sensing of Environment*, *275*, 113013. https://doi.org/10.1016/j.rse.2022.113013

Witkin, A. P. (1987). Scale-space filtering. In *Readings in computer vision* (pp. 329–332). Elsevier.

Yang, Q., Yunjun, Z., & Wang, R. (2024). Heterogeneous InSAR tropospheric correction based on local texture correlation. *IEEE Transactions on Geoscience and Remote Sensing*, *62*, 1–14. https://doi.org/10.1109/TGRS.2024.3356749

Yu, C., Li, Z., & Penna, N. T. (2018). Interferometric synthetic aperture radar atmospheric correction using a GPS-based iterative tropospheric decomposition model. *Remote Sensing of Environment*, *204*, 109–121. https://doi.org/10.1016/j.rse.2017.10.038

Zebker, H. A. (2017). User-friendly InSAR data products: Fast and simple timeseries processing. *IEEE Geoscience and Remote Sensing Letters*, *14*(11), 2122–2126. https://doi.org/10.1109/lgrs.2017.2753580

Zebker, H. A., Rosen, P. A., & Hensley, S. (1997). Atmospheric effects in interferometric synthetic aperture radar surface deformation and topographic maps. *Journal of Geophysical Research*, *102*(B4), 7547–7563. (Publisher: Wiley Online Library. https://doi.org/10.1029/96JB03804

Zebker, H. A., & Villasenor, J. (1992). Decorrelation in interferometric radar echoes. *IEEE Transactions on Geoscience and Remote Sensing*, *30*(5), 950–959. https://doi.org/10.1109/36.175330

Zebker, M. S., Chen, J., & Hesse, M. A. (2023). Robust surface deformation and tropospheric noise characterization from common-reference interferogram subsets. *IEEE Transactions on Geoscience and Remote Sensing*, *61*, 1-1–14. https://doi.org/10.1109/TGRS.2023.3288019

Zhao, Z., Wu, Z., Zheng, Y., & Ma, P. (2021). Recurrent neural networks for atmospheric noise removal from InSAR time series with missing values. *ISPRS Journal of Photogrammetry and Remote Sensing*, *180*, 227–237. https://doi.org/10.1016/j.isprsjprs.2021.08.009

Zheng, Y., & Zebker, H. A. (2017). Phase correction of single-look complex radar images for user-friendly efficient interferogram formation. *IEEE Journal of Selected Topics in Applied Earth Observations and Remote Sensing*, *10*(6), 2694–2701. https://doi.org/10.1109/jstars.2017.2697861

Zwieback, S., & Meyer, F. J. (2022). Reliable InSAR phase history uncertainty estimates. *IEEE Transactions on Geoscience and Remote Sensing*, *60*, 1–9. https://doi.org/10.1109/TGRS.2022.3146816